Solar Phys (2007) 240: 227–239
DOI 10.1007/s11207-006-0266-3

Computing Nonlinear Force-Free Coronal Magnetic Fields in Spherical Geometry

T. Wiegelmann

Received: 11 July 2006 / Accepted: 17 December 2006 /
Published online: 1 March 2007

Abstract We describe a newly developed code for the extrapolation of nonlinear force-free coronal magnetic fields in spherical coordinates. The program uses measured vector magnetograms on the solar photosphere as input and solves the force-free equations in the solar corona. The method is based on an optimization principle and the heritage of the newly developed code is a corresponding method in Cartesian geometry. We test the newly developed code with the help of a semi-analytic solution and rate the quality of our reconstruction qualitatively by magnetic field line plots and quantitatively with a number of comparison metrics. We find that we can reconstruct the original test field with high accuracy. The method is fast if the computation is limited to low co-latitudes (say $30° \leq \theta \leq 150°$), but it becomes significantly slower if the polar regions are included.

1. Introduction

The solar corona is dominated by the coronal magnetic field because the magnetic pressure is several orders of magnitude higher than the plasma pressure. Knowledge regarding the coronal magnetic field is therefore important to understand the structure of the coronal plasma and to get insights regarding dynamical processes such as flares and coronal mass ejections. The direct measurement of magnetic fields is very difficult and such measurements are only occasional available; see, *e.g.*, Lin, Kuhn, and Coulter (2004). Well established are measurements of the photospheric magnetic field with the help of line-of-sight magnetographs (*e.g.*, SOHO/MDI and NSO/Kitt Peak) or vector magnetographs (*e.g.*, currently with the Solar Flare Telescope/NAOJ and the Imaging Vector Magnetograph/Mees Observatory, and in the near future with SOLIS/NSO, Hinode, and SDO/HMI). These photospheric fields can be extrapolated into the solar corona by making suitable model assumptions. The simplest approach is to assume current-free potential fields, which can be computed from the photospheric line-of-sight magnetic field alone. Such source surface potential field models (Schatten, Wilcox, and Ness, 1969; Neugebauer *et al.*, 2002; Schrijver and Derosa, 2003) already

T. Wiegelmann (✉)
Max-Planck-Institut für Sonnensystemforschung, Max-Planck-Strasse 2,
37191 Katlenburg-Lindau, Germany
e-mail: wiegelmann@mps.mpg.de

give some insight about the coronal magnetic field structure, *e.g.*, regarding the location of coronal holes and active regions. They cannot, however, be used to estimate the magnetic energy and helicity of the corona; in particular, they fail to provide an estimate of the free energy available for eruptive phenomena. For reliable estimates of these quantities, currents have to be included. To lowest order the effects of plasma pressure and gravity can be neglected and we can assume that the currents are parallel to the magnetic field, the force-free assumption. A popular simplification of force-free fields are linear force-free fields (Chiu and Hilton, 1977; Seehafer, 1978) where the electric current flow is parallel to the magnetic field with a global constant of proportionality α. This approach is particularly popular because linear force-free models require only line-of-sight magnetograms as input and contain only a single free parameter α, which can be specified by comparing magnetic field line plots with coronal images (Carcedo *et al.*, 2003; Marsch, Wiegelmann, and Xia, 2004). In general α changes in space and taking this into account requires the use of nonlinear force-free models. A comparison of observationally inferred 3D magnetic field structures in a newly developed active region (Solanki *et al.*, 2003) with different extrapolated field models by Wiegelmann *et al.* (2005b) revealed that linear force-free fields are better than potential fields, but nonlinear force-free models are even more accurate. The computation of nonlinear force-free fields is more challenging, however, for several reasons. Mathematically, problems regarding the existence and uniqueness for various boundary value problems dealing with nonlinear force-free fields are still open; see Amari, Boulmezaoud, and Aly (2006) for details. Another issue is the numerical analysis for a given boundary value problem. An additional complication is to derive the required boundary data from photospheric vector magnetic field measurements. High noise in the transversal components of the measured field vector, ambiguities regarding the field direction, and nonmagnetic forces in the photosphere complicate the task to derive suitable boundary conditions from measured data.

Different approaches have been proposed for the nonlinear force-free extrapolation of vector magnetograms:

- The upward integration method (*e.g.*, Wu *et al.*, 1990; Cuperman, Demoulin, and Semel, 1991; Demoulin, Cuperman, and Semel, 1992; Amari *et al.*, 1997)
- The Grad–Rubin-like method (*e.g.*, Grad and Rubin, 1958; Sakurai, 1981; Amari *et al.*, 1997; Amari, Boulmezaoud, and Mikic, 1999; Wheatland, 2004; Amari, Boulmezaoud, and Aly, 2006)
- Different MHD relaxation methods (*e.g.*, Mikic and McClymont, 1994; Roumeliotis, 1996; Valori, Kliem, and Keppens, 2005)
- The Green's-function-like method (*e.g.*, Yan and Sakurai, 2000; Yan and Li, 2006) and
- the optimization method (*e.g.*, Wheatland, Sturrock, and Roumeliotis, 2000; Wiegelmann, 2004)

For a more complete review on existing methods for computing nonlinear force-free coronal magnetic fields see the review papers by Amari *et al.* (1997) and Schrijver *et al.* (2006). The Grad–Rubin method as described in Amari *et al.* (1997) and Amari, Boulmezaoud, and Mikic (1999) has been applied to investigate particular active regions in Bleybel *et al.* (2002) and a comparison of the extrapolated field with 2D projections of plasma structures as seen in Hα, EUV, and X rays has been done in Régnier, Amari, and Kersalé (2002) and Régnier and Amari (2004). The optimization code in the implementation of Wiegelmann (2004) has been applied to an active region in Wiegelmann *et al.* (2005a) and compared with Hα images. Wiegelmann and Inhester (2006) investigated the possibility of using magnetic field extrapolations to improve the stereoscopic 3D reconstruction from coronal images observed from two viewpoints.

Recently, Schrijver *et al.* (2006) compared the performance of six different Cartesian nonlinear force-free extrapolation codes in a blind algorithm test. All algorithms yield nonlinear force-free fields that agree well with the reference field in the deep interior of the volume, where the field and electrical currents are strongest. The optimization approach also successfully reproduced the weak field regions and compute the magnetic energy content correctly with an accuracy of 2%. In a coordinated study Amari, Boulmezaoud, and Aly (2006) obtained an accuracy of somewhat better than 2%.

The good performance of the optimization method encourages us to develop a spherical version of the optimization code. The required full-disk vector magnetograms will become available soon (*e.g.*, from SOLIS). The heritage of the newly developed code is a Cartesian force-free optimization method as implemented by Wiegelmann (2004). We outline the paper as follows. In Section 2 we describe our newly developed algorithm. Section 3 contains a semi-analytic test case and the setup of computations to check the accuracy and performance of our code. We introduce figures of merit to rate the quality of our reconstruction in Section 4 and present the results of our test runs in Section 5. Finally, we draw conclusions in Section 6 and give an outlook for future work.

2. Method

Force-free magnetic fields have to obey the equations

$$(\nabla \times \mathbf{B}) \times \mathbf{B} = \mathbf{0}, \tag{1}$$

$$\nabla \cdot \mathbf{B} = 0. \tag{2}$$

We solve Equations (1) and (2) with the help of an optimization principle as proposed by Wheatland, Sturrock, and Roumeliotis (2000) and generalized by Wiegelmann (2004). Until now the method has been implemented in Cartesian geometry.

Here we define a functional in spherical geometry:

$$L = \int_V \left[B^{-2}\left|(\nabla \times \mathbf{B}) \times \mathbf{B}\right|^2 + |\nabla \cdot \mathbf{B}|^2\right] r^2 \sin\theta \, dr \, d\theta \, d\phi. \tag{3}$$

It is obvious that the force-free equations (1) and (2) are fulfilled when L equals zero. We normalize the magnetic field with the average radial magnetic field on the photosphere and the length scale with a solar radius.

The functional (3) can be numerically minimized with the help of the iteration equations:

$$\frac{\partial \mathbf{B}}{\partial t} = \mu \mathbf{F} \tag{4}$$

where μ is a positive constant and

$$\mathbf{F} = \nabla \times (\boldsymbol{\Omega}_a \times \mathbf{B}) - \boldsymbol{\Omega}_a \times (\nabla \times \mathbf{B}) + \nabla(\boldsymbol{\Omega}_b \cdot \mathbf{B}) - \boldsymbol{\Omega}_b(\nabla \cdot \mathbf{B}) + \left(\boldsymbol{\Omega}_a^2 + \boldsymbol{\Omega}_b^2\right)\mathbf{B} \tag{5}$$

with

$$\boldsymbol{\Omega}_a = B^{-2}\left[(\nabla \times \mathbf{B}) \times \mathbf{B}\right], \tag{6}$$

$$\boldsymbol{\Omega}_b = B^{-2}\left[(\nabla \cdot \mathbf{B})\mathbf{B}\right]. \tag{7}$$

The theoretical deviation of the iterative equation (4) as outlined by Wheatland, Sturrock, and Roumeliotis (2000) does not depend on the use of a specific coordinate system. Previous numerical implementations of this method have been done to our knowledge only in Cartesian geometry, however. Here we describe a newly developed implementation in spherical geometry.

2.1. Implementation

We use a spherical grid r, θ, ϕ with n_r, n_θ, n_ϕ grid points in the radial direction, latitude,[1] and longitude, respectively. Here we intend to compute the whole sphere $r = 1R_s \ldots 2.57R_s$, $\theta = 0^\circ \ldots 180^\circ$, $\phi = 0^\circ \ldots 360^\circ$, but in principle one could limit the method also to parts of a sphere. To avoid the mathematical singularities at the poles, we do not use grid points exactly at the south and north pole, but set them half a grid point apart at $\theta_{\min} = \frac{d\theta}{2}$ and $\theta_{\max} = 180^\circ - \frac{d\theta}{2}$.

The method works as follows:

1. We compute the initial source surface potential field in the computational domain from B_r on the photosphere at $r = 1R_s$.
2. We replace B_θ and B_ϕ at the bottom photospheric boundary at $r = 1R_s$ by the measured vector magnetogram.[2] The outer radial boundary is unchanged from the initial potential field model. For the purpose of code testing we also try other additional boundary conditions (see Section 3.2).
3. We iterate for a force-free magnetic field in the computational box by minimizing the functional L of (3) by applying (4).
4. The continuous form of (4) ensures a monotonically decreasing functional L. For finite time steps, this is also ensured if the iteration time step dt is sufficiently small. If $L(t + dt) \geq L(t)$ this step is rejected and we repeat this step with dt reduced by a factor of 2.
5. After each successful iteration step we increase dt by a factor of 1.01 to ensure a time step as large as possible within the stability criteria. This ensures an iteration time step close to its optimum.
6. The iteration stops if dt becomes too small. As stopping criteria we use $dt \leq 10^{-9}$.

[1] θ corresponds to the co-latitude, with $\theta = 0^\circ$ and $\theta = 180^\circ$ at the south and north poles, respectively.

[2] It is as well possible to replace only parts of the photosphere (a limited region in θ and ϕ direction) and to restrict the nonlinear force-free computation onto this region. This is in particular necessary if the observed photospheric vector magnetogram is only available for parts of the photosphere. In such cases the global magnetic field is basically a potential field and only locally (say, in active regions) a nonlinear force-free field. For such limited regions in θ and ϕ we encounter the same problem as in Cartesian codes: that the lateral boundary conditions are unknown. One possibility is to describe the lateral boundaries with the help of a global potential field. The assumption of a potential field outside the computational domain restricts currents to the active region, but non-current-carrying field lines can leave the computational box. At the interface between the potential and non-potential field, a boundary layer as described in Wiegelmann (2004) for the Cartesian implementation of our code can be used. Full spherical force-free fields certainly do not have lateral boundaries and if one is interested in the details of interaction of two far-apart active regions, it might be better to compute first a global low-resolution force-free field (*e.g.*, in future with SOLIS data) and then compute the field in the active regions with higher resolution (*e.g.*, with Hinode data). Such an approach would also allow current-carrying field lines to connect the two active regions, which might be important for the initiation of CMEs.

3. Test Case

3.1. Semi-Analytic Reference Field

We test our newly developed code with the help of a known nonlinear force-free field model developed by Low and Lou (1990). The authors solved the Grad – Shafranov equation for axisymmetric force-free fields in spherical coordinates r, θ, ϕ. The magnetic field can be written in the form

$$\mathbf{B} = \frac{1}{r\sin\theta}\left(\frac{1}{r}\frac{\partial A}{\partial \theta}\mathbf{e}_r - \frac{\partial A}{\partial r}\mathbf{e}_\theta + Q\mathbf{e}_\phi\right) \tag{8}$$

where A is the flux function and Q represents the ϕ-component of $\mathbf{B}$, depending only on A. The flux function A satisfies the Grad – Shafranov equation

$$\frac{\partial^2 A}{\partial r^2} + \frac{1-\mu^2}{r^2}\frac{\partial^2 A}{\partial \mu^2} + Q\frac{dQ}{dA} = 0 \tag{9}$$

where $\mu = \cos\theta$. Low and Lou (1990) derive solutions for

$$\frac{dQ}{dA} = \alpha = \text{const.} \tag{10}$$

by looking for separable solutions of the form

$$A(r,\theta) = \frac{P(\mu)}{r^n}. \tag{11}$$

The solutions are axisymmetric in spherical coordinates with a point source at the origin. They have become a kind of standard test for nonlinear force-free extrapolation codes (Amari, Boulmezaoud, and Mikic, 1999; Wheatland, Sturrock, and Roumeliotis, 2000; Wiegelmann and Neukirch, 2003; Yan and Li, 2006; Amari, Boulmezaoud, and Aly, 2006; Inhester and Wiegelmann, 2006; Schrijver *et al.*, 2006) in Cartesian geometry because the symmetry in the solution is no longer obvious after a translation that places the point source outside the computational domain and a rotation of the symmetry axis with respect to the Cartesian coordinate axis.

Here we use the Low and Lou solution in spherical coordinates. The original equilibrium is invariant in ϕ, but we can produce a 3D-looking configuration by placing the origin of the solution with 1/4 solar radius offset to the sun center. The corresponding configuration is no longer symmetric in ϕ with respect to the solar surface, as seen in the synoptic map in Figure 1, which shows B_r on the photosphere. Let us remark that we use the solution for the purpose of testing our code only and the equilibrium is not assumed to be a realistic model for the global coronal magnetic field. We do the test runs on spherical grids (r, θ, ϕ) of $20 \times 40 \times 80$ and $40 \times 80 \times 160$ grid points.

3.2. Boundary Conditions

- Case 1: The boundary is specified on the photosphere, on the source surface, and in co-latitude at $\theta = 30°$ and $\theta = 150°$. Optimization is restricted in co-latitude to $30° < \theta < 150°$.
- Case 2: The boundary is specified on the photosphere, on the source surface, and in co-latitude at $\theta = \frac{d\theta}{2}$ and $\theta = 180° - \frac{d\theta}{2}$.

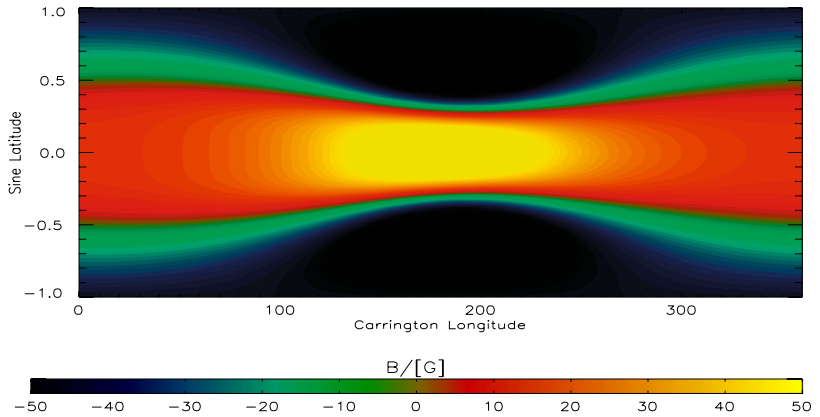

Figure 1 The synoptic map of B_r on the photosphere. We project the map onto the solar surface in Figure 2 with the disk center at Carrington longitude 180°.

– Case 3: The boundary is specified on the photosphere and on the source surface.
– Case 4: The boundary is specified only on the photosphere. This is the realistic case for real data, where measurements are only available on the photosphere. On the source surface the magnetic field is chosen from the initial potential field.

For the computations done here we use a grid resolution of $d\theta = d\phi = 4.5°$ for the low-resolution test case and $d\theta = d\phi = 2.25°$ for the high-resolution one.[3] This means that the full spherical extrapolation cases (Cases 2–4) are limited in co-latitude by $2.25° \leq \theta \leq 177.75°$ and $1.125° \leq \theta \leq 178.875°$ for the low- and high-resolution computations, respectively. As the initial state we compute a source surface potential field in our computational domain. The source surface is a spherical shell where all field lines are assumed to become radial (Schatten, Wilcox, and Ness, 1969). We locate the source surface at $1 + \frac{\pi}{2} \approx 2.57 R_s$, which is the outer radial boundary of our physical domain. The finite differences in ϕ are cyclic. For Cases 1 and 2 boundary values in θ are specified and for Cases 3 and 4 we interpolate the values at the poles.

4. Figures of Merit

In Table 1 we provide some quantitative measures to rate the quality of our reconstruction. Column 1 names the corresponding test case. Columns 2–4 show how well the force and solenoidal condition are fulfilled, where column 2 contains the value of the functional L as defined in (3) and L_1 and L_2 in columns 3 and 4 correspond to the first (force-free) and second (solenoidal free) part of L. The evolution of the functional L during the optimization process is shown in Figure 3. Column 5 contains the L_∞ norm of the divergence of the magnetic field:

$$\|\nabla \cdot \mathbf{B}\|_\infty = \sup_{\mathbf{x} \in V} |\nabla \cdot \mathbf{B}|, \tag{12}$$

[3] If the angle is given in radians we have $dr = d\theta = d\phi$ for the test cases. The code also allows, however, the use of $dr \neq d\theta \neq d\phi$.

Table 1 Quality of our reconstructions with several figures of merit as explained in Section 4.

Model	L	L_1	L_2	$\|\nabla \cdot \mathbf{B}\|_\infty$	$\|\mathbf{j} \times \mathbf{B}\|_\infty$	C_{vec}	C_{CS}	E_{N}	E_{M}	ϵ	Steps	Time
	Spherical grid $20 \times 40 \times 80$											
Original	0.04	0.03	0.01	0.48	1.37	1	1	0	0	1		
Potential	0.19	0.006	0.13	4.61	0.90	0.66	0.77	0.71	0.68	0.75		
Case 1	0.014	0.010	0.004	0.42	0.64	0.9998	0.9995	0.012	0.016	1.008	1889	2 min
Case 2	0.013	0.010	0.003	0.42	0.64	0.9998	0.9992	0.016	0.023	1.007	31129	23 min
Case 3	0.23	0.20	0.03	3.00	11.30	0.998	0.998	0.04	0.05	0.99	23824	18 min
Case 4	0.48	0.34	0.14	3.11	11.30	0.993	0.95	0.14	0.29	0.95	10167	7 min
	Spherical grid $40 \times 80 \times 160$											
Original	0.005	0.003	0.002	0.38	0.71	1	1	0	0	1		
Potential	0.30	0.0003	0.30	0.44	0.23	0.67	0.77	0.70	0.67	0.75		
Case 1	0.0016	0.0010	0.0006	0.38	0.32	0.99998	0.99989	0.004	0.007	1.002	14522	1 h 26 min
Case 2	0.0027	0.0020	0.0007	0.40	0.53	0.99992	0.9995	0.011	0.019	0.9989	672281	65 h 19 min
Case 3	0.24	0.20	0.04	6.63	22.47	0.996	0.99	0.086	0.12	0.96	171143	16 h 57 min
Case 4	0.39	0.27	0.12	6.60	22.47	0.99	0.93	0.17	0.32	0.92	120742	12 h 00 min

We compute the figures for the whole sphere. For Case 1, where the computations have been limited in latitude, the reference field was specified in the cones $\theta < 30°$ and $\theta > 150°$.

and column 6 lists the L_∞ norm of the Lorentz force of the magnetic field:

$$\|\mathbf{j}\times\mathbf{B}\|_\infty = \sup_{\mathbf{x}\in V}|\mathbf{j}\times\mathbf{B}|. \tag{13}$$

The next five columns of Table 1 contain different measures that compare our reconstructed field with the semi-analytic reference field. These measures have been introduced by Schrijver *et al.* (2006) to compare a vector field $\mathbf{b}$ with a reference field $\mathbf{B}$.

– Column 7 lists the vector correlation

$$C_{\rm vec} = \sum_i \mathbf{B}_i\cdot\mathbf{b}_i \Big/ \left(\sum_i |\mathbf{B}_i|^2 \sum_i |\mathbf{b}_i|^2\right)^{1/2}. \tag{14}$$

– Column 8 lists the Cauchy–Schwarz inequality

$$C_{\rm CS} = \frac{1}{N}\sum_i \frac{\mathbf{B}_i\cdot\mathbf{b_i}}{|\mathbf{B}_i||\mathbf{b}_i|} \tag{15}$$

where N is the number of vectors in the field.

– Column 9 lists the normalized vector error

$$E_{\rm N} = \sum_i |\mathbf{b}_i-\mathbf{B}_i| \Big/ \sum_i |\mathbf{B}_i|. \tag{16}$$

– Column 10 lists the mean relative vector error

$$E_{\rm M} = \frac{1}{N}\sum_i \frac{|\mathbf{b}_i-\mathbf{B}_i|}{|\mathbf{B}_i|}. \tag{17}$$

– Column 11 lists the total magnetic energy of the reconstructed field normalized with the energy of the input field:

$$\epsilon = \frac{\sum_i |\mathbf{b}_i|^2}{\sum_i |\mathbf{B}_i|^2}. \tag{18}$$

The two vector fields agree perfectly if $C_{\rm vec}$, $C_{\rm CS}$, and ϵ are unity and if $E_{\rm N}$ and $E_{\rm M}$ are zero. Column 12 contains the number of iteration steps until convergence and column 13 shows the computing time on four processors.

5. Results

5.1. Qualitative Comparison

In Figure 2 we compare magnetic field line plots of the original model field (Original) with a corresponding potential field (Potential) and nonlinear force-free reconstructions with different boundary conditions (Cases 1 – 4). The color coding shows the radial magnetic field on the photosphere, as also shown in the synoptic map in Figure 1. Carrington longitude 180° corresponds to the disk center in Figure 2. The images show the results of the computation on the $20\times 40\times 80$ grid.

A comparison of the original reference field (Original in Figure 1) with our nonlinear force-free reconstructions (Cases 1 – 4) shows that the magnetic field line plots agree with

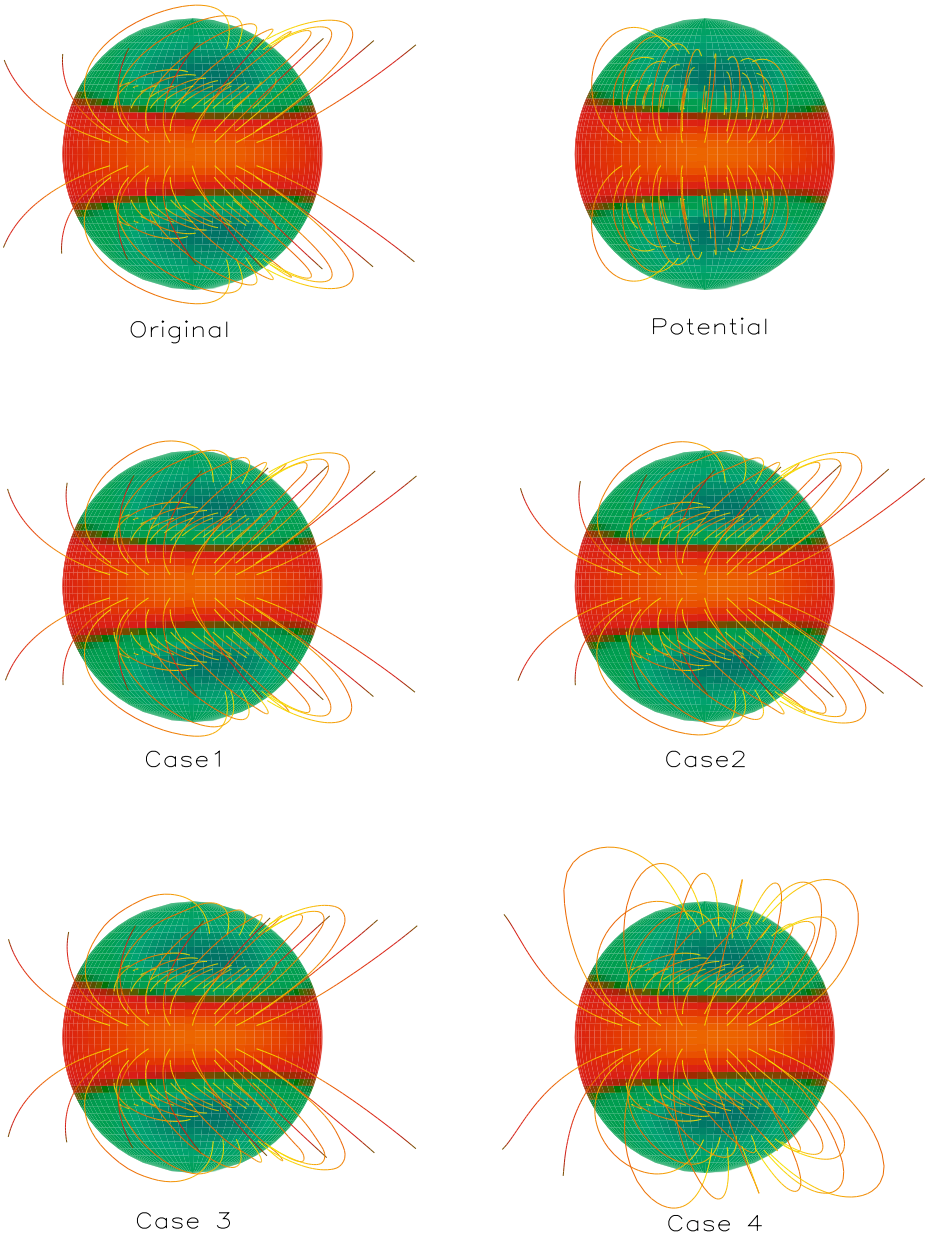

Figure 2 The original reference field, a global potential field, and the results of a nonlinear force-free reconstruction with different boundary conditions (Cases 1 – 4; see text). The color coding shows B_r on the photosphere and the disk center corresponds to 180° longitude.

the original for Case 1 – 3 within the plotting precision. Case 4 shows some deviations from the original, but the reconstructed field lines are much closer to the reference field than to the initial potential field (Potential). We cannot expect a perfect agreement with the reference

field for Case 4, because here the outer radial boundary conditions are taken from the initial potential field model, which are different from the outer boundary of the reference field. It is well known from computations in Cartesian geometry that the lateral and top boundaries influence the solution in the box.[4]

5.2. Quantitative Comparison

The visual inspection of Figure 2 is supported by the quantitative criteria shown in Table 1. For Cases 1 and 2 (where the boundary conditions have been specified on the photosphere, on the source surface, and in latitude) the formal force-free criteria (L, L_1, L_2) are smaller than the discretization error of the analytic solution and the comparison metrics show an almost perfect agreement with the reference field. For Case 3 we still find a very good agreement between the reference field and our reconstruction and for Case 4 the agreement is still reasonable. We are in particular able to correctly compute the magnetic energy content of the coronal magnetic field approximately. A potential field reconstruction does obviously not agree with the reference field. The figures of merit show that the potential field is far away from the true solutions and contains only 75% of the magnetic energy.

For a practical use of any numerical scheme the computing time certainly matters. As seen in the last column of Table 1 the computing time is quite fast if we restrict the computational domain to low co-latitudes ($30^\circ < \theta < 150^\circ$, Case 1) but increases significantly for full-sphere computations. The time needed for one iterative time step is approximately constant (0.04 s on the low-resolution grid and 0.36 s on the high-resolution one), but the number of iteration steps needed until convergence increases by more than one order of magnitude if high co-latitude regions are included in the optimization. The reason is that the iteration time step dt, which adjusts automatically in our code, becomes much smaller and consequently the convergence speed becomes slow. This is quite visible in Figure 3, which shows the evolution of the functional L with the number of iteration steps. For the low-latitude computations (Case 1, solid line in Figure 3) the functional L is much steeper than for the full-sphere computations (Cases 2 – 4, dotted, dashed, and dash-dotted lines). The slow convergence of the full-sun computations is directly related to the smaller time step and the time step itself is restricted by the physical grid resolution,[5] which becomes very small close to the poles. We will address this point in the discussion (Section 6) and outline possible solutions to overcome these difficulties.

Some insights regarding the performance of our newly developed code might be given by a comparison of the figures in Table 1 with the results of computations in Cartesian coordinates, as shown in of Schrijver *et al.* (2006), where row (b) contains the results of our Cartesian optimization code. The upper part of Schrijver's Table I corresponds to a test case where all six boundaries of a Cartesian box have been specified (Schrijver's Case I, which is somewhat similar to our Cases 1 – 3) and the lower part of Schrijver's Table I corresponds to a case where only the bottom boundary of a Cartesian box has been specified (Schrijver's Case II, which is equivalent to our Case 4 in spherical geometry). Both for Cartesian and spherical computations the correspondence with the original field is reduced if the boundary conditions are only specified on the photosphere. For real observed vector magnetograms we certainly have only photospheric data and it is therefore important to get a reasonable

[4] In the Cartesian case this effect can be reduced by choosing a well-isolated active region surrounded by a sufficiently large area with low magnetic field; see, *e.g.*, test case II in Schrijver *et al.* (2006).

[5] This condition is similar to the CFL condition for time-dependent problems.

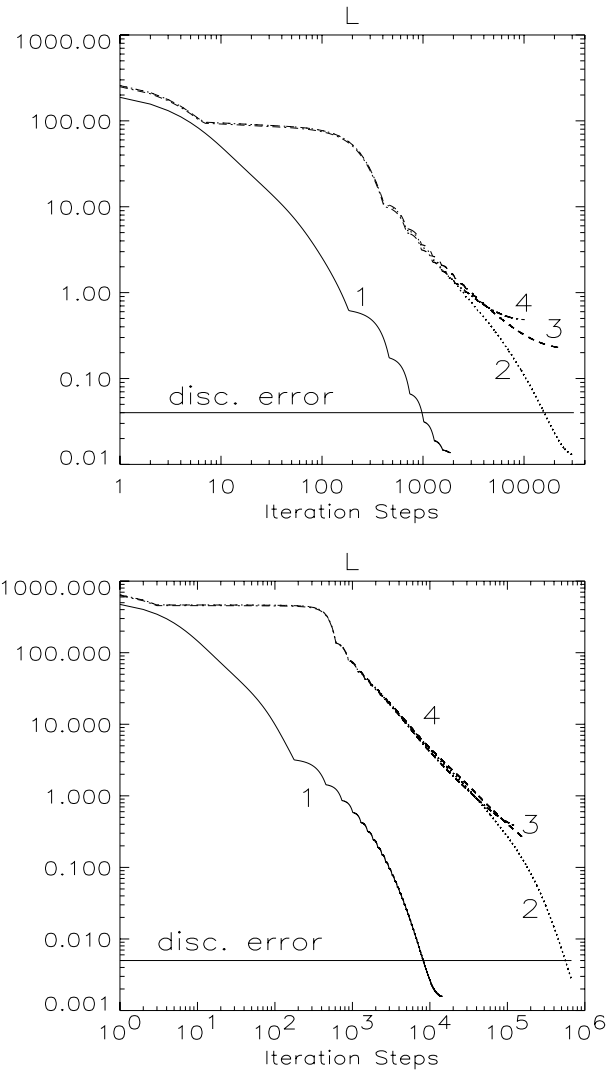

Figure 3 Evolution of L (as defined in 3) during the optimization process. The solid line corresponds to Case 1, the dotted line to Case 2, the dashed line to Case 3, and the dash-dotted line to Case 4. The horizontal dash-double-dotted line marks the discretization error of the original semi-analytic solution. The top panel corresponds to the low-resolution ($20 \times 40 \times 80$) and the bottom panel to the high-resolution ($40 \times 80 \times 160$) computation.

nonlinear force-free magnetic field reconstruction for this case. The errors of the different comparison metrics are still small and in a comparable range for Cartesian and spherical computations. The vector correlation is better than 99% and we got the magnetic energy correct within a few percent for all examples investigated in this paper.

6. Discussion and Outlook

Within this work we developed a code for the nonlinear force-free computation of coronal magnetic fields in spherical geometry. The method is based on an optimization principle. We tested the performance of the newly developed code with the help of a semi-analytic reference field. We find that the spherical optimization method works well and the accuracy

of the reconstructed magnetic field configuration is comparable with the performance of a corresponding code in Cartesian geometry. The computation is reasonably fast if we limit the computation to low-latitude regions but becomes significantly slower if polar regions are included. Such a behavior is well known for computations in spherical coordinates; see, *e.g.*, Kageyama and Sato (2004). This is because the physical grid converges to the poles. A fair approximation for the iteration time step is $dt \propto \Delta^2$, where Δ is the physical grid resolution. As the finest grid resolution restricts the time step, it becomes much smaller if high-altitude regions (where Δ becomes very small) are included in the optimization. Our code has an automatic step size control and we find that dt automatically adjusts to much smaller values for full-sphere computations.

A possible solution is the use of the so-called Yin – Yang grid, as developed by Kageyama and Sato (2004) and as used, *e.g.*, for Earth mantle convection by Yoshida and Kageyama (2004). The Yin – Yang grid is composed of two identical complementary grids, which partly overlap and together cover the solar surface with a quasi-uniform grid spacing (see Kageyama and Sato, 2004 for details). Naturally, the Yin – Yang grid has no poles at all and a considerably large iteration step can be used. There is certainly a numerical overhead for transformations between the complementary grids, but the limitations regarding the time step in polar regions for traditional spherical grids are more time demanding. For solar applications one has to consider, however, that photospheric magnetic field measurements are currently less accurate close to the poles. It might therefore be acceptable to restrict nonlinear force-free computations onto equatorial regions, say between about 30° and 150° latitude.[6] For these low-latitude regions the spherical optimization code as described here is reasonably fast. For application to observed vector magnetograms one has to consider that the measured magnetic field is not necessary force-free in the photosphere and in particular the transverse components of the magnetic field vector contain considerable noise. These problems are, however, also present for force-free extrapolations in Cartesian geometry and a preprocessing of the photospheric vector magnetograms as described in Wiegelmann, Inhester, and Sakurai (2006) helps to overcome these difficulties.

The code solves the nonlinear force-free equations in the bounded domain between $1R_\mathrm{s}$ and the source surface at $2.57R_\mathrm{s}$. The outer boundary is kept fixed from the initial potential field. All current-carrying field lines have to close inside the volume. The domain outside $2.57R_\mathrm{s}$ is not included in the model, because the force-free approach is no longer justified here. A further step toward a consistent modeling of the solar corona would be the inclusion of non-magnetic forces, such as plasma pressure, gravity, and the dynamic pressure of the solar wind. This is particularly useful for long structures of several solar radii, such as helmet streamers, where the plasma β becomes finite (see, *e.g.*, Guo and Wu, 1998 and Wiegelmann, Schindler, and Neukirch, 1998). Neukirch (1995) found a special class of magnetohydrostatic solutions that are separable in spherical coordinates. Petrie and Neukirch (2000) extended the linear force-free Green's function methods to include non-magnetic forces in Cartesian geometry. Both approaches assume a kind of global linear force-free parameter α for the parallel part of the electric currents. This is certainly a too restrictive condition to include the detailed information provided by measured vector magnetograms. The optimization method has been generalized for this aim in Wiegelmann and Inhester (2003) and implemented in Cartesian geometry. A corresponding implementation into spherical geometry is straightforward but does certainly require additional observational constraints (*e.g.*, the tomographically reconstructed 3D coronal density distribution).

[6] Alternatively, one could use a larger grid spacing for the computation of a force-free field in polar regions.

Acknowledgements This work was supported by DLR Grant No. 50 OC 0501. The author thanks Bernd Inhester for useful comments and acknowledges inspiring discussions on three workshops organized by Karel Schrijver (NLFFF Consortium) in Palo Alto between 2004 and 2006. We thank the referee, Tahar Amari, for useful remarks to improve this paper.

References

Amari, T., Boulmezaoud, T.Z., Aly, J.J.: 2006, *Astron. Astrophys.* **446**, 691.
Amari, T., Boulmezaoud, T.Z., Mikic, Z.: 1999, *Astron. Astrophys.* **350**, 1051.
Amari, T., Aly, J.J., Luciani, J.F., Boulmezaoud, T.Z., Mikic, Z.: 1997, *Solar Phys.* **174**, 129.
Bleybel, A., Amari, T., van Driel-Gesztelyi, L., Leka, K.D.: 2002, *Astron. Astrophys.* **395**, 685.
Carcedo, L., Brown, D.S., Hood, A.W., Neukirch, T., Wiegelmann, T.: 2003, *Solar Phys.* **218**, 29.
Chiu, Y.T., Hilton, H.H.: 1977, *Astrophys. J.* **212**, 873.
Cuperman, S., Demoulin, P., Semel, M.: 1991, *Astron. Astrophys.* **245**, 285.
Demoulin, P., Cuperman, S., Semel, M.: 1992, *Astron. Astrophys.* **263**, 351.
Grad, H., Rubin, H.: 1958, In: *Proceedings of the 2nd International Conference on Peaceful Uses of Atomic Energy* **31**, United Nations, Geneva, 190.
Guo, W.P., Wu, S.T.: 1998, *Astrophys. J.* **494**, 419.
Inhester, B., Wiegelmann, T.: 2006, *Solar Phys.* **235**, 201.
Kageyama, A., Sato, T.: 2004, *Geochem. Geophys. Geosyst.* **5**, 9005.
Lin, H., Kuhn, J.R., Coulter, R.: 2004, *Astrophys. J.* **613**, L177.
Low, B.C., Lou, Y.Q.: 1990, *Astrophys. J.* **352**, 343.
Marsch, E., Wiegelmann, T., Xia, L.D.: 2004, *Astron. Astrophys.* **428**, 629.
Mikic, Z., McClymont, A.N.: 1994, In: Balasubramaniam, K.S., Simon, G.W. (eds.) *Solar Active Region Evolution: Comparing Models with Observations*, *Astron. Soc. Pacific Conf. Ser.* **68**, 225.
Neugebauer, M., Liewer, P.C., Smith, E.J., Skoug, R.M., Zurbuchen, T.H.: 2002, *J. Geophys. Res.* **107**(13), 1.
Neukirch, T.: 1995, *Astron. Astrophys.* **301**, 628.
Petrie, G.J.D., Neukirch, T.: 2000, *Astron. Astrophys.* **356**, 735.
Régnier, S., Amari, T.: 2004, *Astron. Astrophys.* **425**, 345.
Régnier, S., Amari, T., Kersalé, E.: 2002, *Astron. Astrophys.* **392**, 1119.
Roumeliotis, G.: 1996, *Astrophys. J.* **473**, 1095.
Sakurai, T.: 1981, *Solar Phys.* **69**, 343.
Schatten, K.H., Wilcox, J.M., Ness, N.F.: 1969, *Solar Phys.* **6**, 442.
Schrijver, C.J., Derosa, M.L.: 2003, *Solar Phys.* **212**, 165.
Schrijver, C.J., Derosa, M.L., Metcalf, T.R., Liu, Y., McTiernan, J., Régnier, S., Valori, G., Wheatland, M.S., Wiegelmann, T.: 2006, *Solar Phys.* **235**, 161.
Seehafer, N.: 1978, *Solar Phys.* **58**, 215.
Solanki, S.K., Lagg, A., Woch, J., Krupp, N., Collados, M.: 2003, *Nature* **425**, 692.
Valori, G., Kliem, B., Keppens, R.: 2005, *Astron. Astrophys.* **433**, 335.
Wheatland, M.S.: 2004, *Solar Phys.* **222**, 247.
Wheatland, M.S., Sturrock, P.A., Roumeliotis, G.: 2000, *Astrophys. J.* **540**, 1150.
Wiegelmann, T.: 2004, *Solar Phys.* **219**, 87.
Wiegelmann, T., Inhester, B.: 2003, *Solar Phys.* **214**, 287.
Wiegelmann, T., Inhester, B.: 2006, *Solar Phys.* **236**, 25.
Wiegelmann, T., Neukirch, T.: 2003, *Nonlinear Process. Geophys.* **10**, 313.
Wiegelmann, T., Schindler, K., Neukirch, T.: 1998, *Solar Phys.* **180**, 439.
Wiegelmann, T., Inhester, B., Sakurai, T.: 2006, *Solar Phys.* **233**, 215.
Wiegelmann, T., Inhester, B., Lagg, A., Solanki, S.K.: 2005a, *Solar Phys.* **228**, 67.
Wiegelmann, T., Lagg, A., Solanki, S.K., Inhester, B., Woch, J.: 2005b, *Astron. Astrophys.* **433**, 701.
Wu, S.T., Sun, M.T., Chang, H.M., Hagyard, M.J., Gary, G.A.: 1990, *Astrophys. J.* **362**, 698.
Yan, Y., Li, Z.: 2006, *Astrophys. J.* **638**, 1162.
Yan, Y., Sakurai, T.: 2000, *Solar Phys.* **195**, 89.
Yoshida, M., Kageyama, A.: 2004, *Geophys. Res. Lett.* **31**, 12609.